2015 IEEE International Conference on Robotics and Automation (ICRA)
Washington State Convention Center
Seattle, Washington, May 26-30, 2015

On Some Practical Reactionless Motion Tasks With a Free-Floating Space Robot

Hiroki Sone and Dragomir N. Nenchev

Abstract— **This work describes how to use reactionless motion control with a free-floating space robot, suggesting thereby some tasks of practical importance. We show that the reactionless motion capability is directly affected by the kinematic structure of the manipulator, depending thereby upon the existence of kinematic redundancy, a typical lower/upper arm subchain and joint offsets. We investigate a seven-DoF redundant manipulator comprising these features and show that approximate reactionless motions can be obtained with the elbow joint only and/or the wrist joints. Using these reactionless motions, we propose three practical maneuvers for eye-in-hand type inspection, arm deploying/stowing and point-to-point motions with partial reactionless motion. Feasibility is verified via numerical simulations.**

I. Introduction

Free-floating space robots are expected to play an important role in such missions as inspection, construction, assembly and debris removal. In order to realize such missions, the robot controller has to deal with the problem of dynamic coupling between the manipulator and the floating satellite base [1]. It is known that the conventional attitude control system based on reaction wheels has limited capabilities w.r.t. base attitude disturbances induced by manipulator motions. To avoid saturation of the reaction wheel signals, the manipulator has to be driven at very low speed. This is not desirable from the perspective of work efficiency and time critical tasks. Therefore, the dynamic coupling and reaction control of the manipulator are as important as its end-effector motion/force control.

The Reaction Null Space (RNS) control method provides a straightforward approach to reactionless motion generation [2], [3]. Therein, the condition for reactionless motion is derived from the angular momentum conservation law. The method has been confirmed by on-orbit experiments with the Engineering Test Satellite VII (ETS-VII) [4], [5]. RNS-based reactionless motion control has been considered also in [6]–[9]. It should be noted, however, that there is a difficulty when applying the method for practical tasks. The reason is the occurrence of complex singularities, when end-effector trajectory tracking control is combined with reactionless motion control. In a previous study [10], it was indicated that such singularities could restrict the motion range of the end-effector while tracking linear paths.

In this work, we identify some practical tasks suitable for execution under reactionless motion control. Thereby, the linear end-effector motion constraint will be relaxed. Also, it will be clarified that the kinematic and dynamic features should be considered with great care. Indeed, it has been argued that special manipulator design can alleviate the dynamical coupling/reaction problem [11], [12]. No feasible designs for free-floating space robots have appeared so far. Here, we consider a structure that is typical for a space manipulator, such as the FREND Robotic Arm [13]. A seven-DoF structure is known to comprise a wider reactionless motion range than the six-DoF manipulator used in the ETS-VII experiments [5], [14]. We identify the following application tasks as prospective from the viewpoint of reactionless motion execution: (i) eye-in-hand inspection, (ii) manipulator deploying/stowing, and (iii) point-to-point (PTP) transport maneuvers with partial reactionless motion. Among these tasks, only the last one has been considered for reactionless motion control, though with a flexible-base robot [15].

The authors are with the Graduate School of Engineering, Tokyo City University, Tamazutsumi 1-28-1, Setagaya-ku, Tokyo 158-8557, Japan. Corresponding author: D. Nenchev (Y. Kanamiya) nenchev@tcu.ac.jp

II. Basic Notation

A. Momentum Conservation

We consider a free-floating space robot model consisting of a satellite base and a serial manipulator arm of n-DoF. It is assumed that external forces and moments are negligible, and hence, the linear and angular momenta are strictly conserved. The dynamic behavior of the system is completely described by the momentum conservation law [16]:

$$\begin{bmatrix} \boldsymbol{p} \\ \boldsymbol{l}_b \end{bmatrix} = \begin{bmatrix} \boldsymbol{M}_v & \boldsymbol{M}_{v\omega} \\ \boldsymbol{M}_{v\omega}^T & \boldsymbol{M}_\omega \end{bmatrix} \begin{bmatrix} \boldsymbol{v}_b \\ \boldsymbol{\omega}_b \end{bmatrix} + \begin{bmatrix} \boldsymbol{M}_{vm} \\ \boldsymbol{M}_{\omega m} \end{bmatrix} \dot{\boldsymbol{\theta}}, \qquad (1)$$

where $\boldsymbol{p}$, $\boldsymbol{l}_b \in \mathbb{R}^3$ denote linear and angular momentum w.r.t. the center of mass (CoM) of the base, $\boldsymbol{v}_b$, $\boldsymbol{\omega}_b \in \mathbb{R}^3$, stand for linear and angular velocity of the base, and $\boldsymbol{\theta} \in \mathbb{R}^n$ is the joint coordinate vector. $\boldsymbol{M}_v$, $\boldsymbol{M}_\omega$, $\boldsymbol{M}_{v\omega} \in \mathbb{R}^{3\times 3}$ are submatrices of the composite-rigid-body (CRB) inertia matrix, $\boldsymbol{M}_{vm}$, $\boldsymbol{M}_{\omega m} \in \mathbb{R}^{3\times n}$ denote inertia submatrices related to the dynamic coupling between the base and the manipulator. These matrices are referred to as the *coupling inertia matrices*. Zero initial momenta were assumed.

The angular momentum conservation law, especially, is of primary importance. Indeed, it has been noted that even slight variations of the base attitude may cause a failure in the communication between the robot and the ground control center. The angular momentum conservation law can be written in the following form [5]:

$$\boldsymbol{0} = \tilde{\boldsymbol{M}}_\omega \boldsymbol{\omega}_b + \tilde{\boldsymbol{M}}_{\omega m} \dot{\boldsymbol{\theta}} \qquad (2)$$

where $\tilde{\boldsymbol{M}}_\omega = \boldsymbol{M}_\omega - \boldsymbol{M}_{v\omega}^T \boldsymbol{M}_v^{-1} \boldsymbol{M}_{v\omega}$ and $\tilde{\boldsymbol{M}}_{\omega m} = \boldsymbol{M}_{\omega m} - \boldsymbol{M}_{v\omega}^T \boldsymbol{M}_v^{-1} \boldsymbol{M}_{vm}$. The first term of the r.h.s. of (2) is the partial angular momentum stemming from base rotation, The

second term, on the other hand, results from manipulator motion; it represents the base disturbance in terms of velocity. This term is referred to as the *coupling angular momentum*.

B. Reactionless motion: The Reaction-Null Space

Reactionless motions are variations of the manipulator configuration that conserve a zero initial base angular momentum throughout the entire motion. This implies $\boldsymbol{\omega}_b = \mathbf{0}$, and hence,

$$\tilde{\boldsymbol{M}}_{\omega m}\dot{\boldsymbol{\theta}} = \mathbf{0}. \tag{3}$$

From this equation, the set of reactionless motions can be represented as [14]:

$$\dot{\boldsymbol{\theta}} = \boldsymbol{P}_{RNS}\dot{\boldsymbol{\theta}}_a, \tag{4}$$

where $\boldsymbol{P}_{RNS} = \boldsymbol{E} - \tilde{\boldsymbol{M}}^{+}_{\omega m}\tilde{\boldsymbol{M}}_{\omega m} \in \mathbb{R}^{n\times n}$ denotes a projector onto the null space of the coupling inertia matrix, $\boldsymbol{E}$ is the identity matrix and $(\circ)^{+}$ stands for the pseudoinverse matrix. $\dot{\boldsymbol{\theta}}_a$ is an arbitrary vector with the dimension of joint velocity. It plays the role of a vector-parameter for the set of reactionless motions. The main concern is how to determine this vector. It is apparent that the null space of the coupling inertia matrix, referred henceforth as the *Reaction-Null Space* (RNS), plays an important role for reactionless motion generation.

In order to generate feasible reactionless motions for a given end-effector path, it is necessary to ensure a RNS of the highest possible dimension. One possibility to increase the dimension is to honor end-effector position

$$\dot{\boldsymbol{\theta}}^{ref} = \begin{bmatrix}\tilde{\boldsymbol{M}}_{\omega m}\\ \boldsymbol{J}_{Ev}\end{bmatrix}^{+}\begin{bmatrix}\mathbf{0}\\ \boldsymbol{v}_E^{ref}\end{bmatrix}, \tag{5}$$

or orientation

$$\dot{\boldsymbol{\theta}}^{ref} = \begin{bmatrix}\tilde{\boldsymbol{M}}_{\omega m}\\ \boldsymbol{J}_{E\omega}\end{bmatrix}^{+}\begin{bmatrix}\mathbf{0}\\ \boldsymbol{\omega}_E^{ref}\end{bmatrix}, \tag{6}$$

only. Here, $\boldsymbol{v}_E$, $\boldsymbol{\omega}_E \in \mathbb{R}^3$ are the linear and angular velocity of the end-effector w.r.t. the base, and $\boldsymbol{J}_{Ev}$, $\boldsymbol{J}_{E\omega} \in \mathbb{R}^{3\times n}$ are the respective Jacobian matrices. It must be noted that this approach introduces the so-called algorithmic singularities that hinder the process of differential motion generation. Especially in the case of (5), these singularities are of complex nature; they depend upon the instantaneous manipulator configuration and the desired end-effector trajectory. Hence, it is impossible to predict the motion range of the manipulator, though it is known to be quite narrow [10]. On the other hand, (6) has been considered in off-line reactionless motion generation with ETS-VII, but only with a constant angular velocity $\boldsymbol{\omega}_E = \text{const.}$ [5]. Our preliminary research results suggest that the algorithmic singularities associated with (6) do not occur as frequently as those with the linear end-effector constraint (5). Therefore, we will propose below a reactionless application task based on (6).

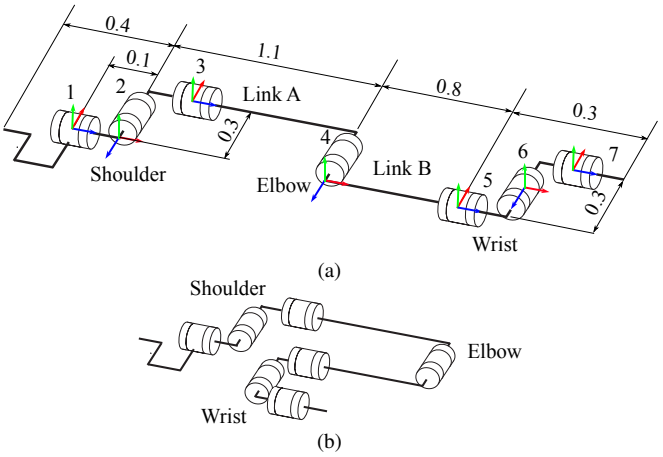

Fig. 1. Seven-DoF redundant manipulator: (a) kinematic structure and (b) stowed configuration.

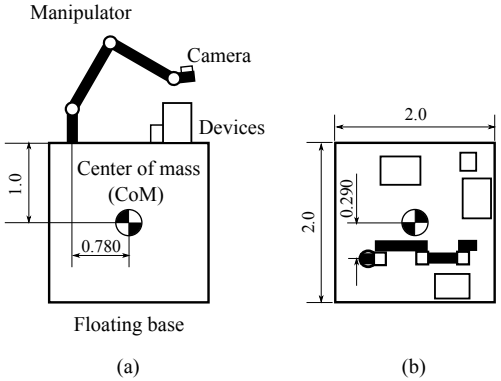

Fig. 2. The seven-DoF manipulator attached to the satellite base: (a) side view and (b) top view. Attachment position and dimensions are based on the ETS-VII design [17].

III. Manipulator Model and Reactionless Motion Analysis

A. Manipulator model

We consider a free-floating space robot comprising a seven-DoF redundant manipulator mounted on a satellite base. The manipulator is characterized by a kinematic chain with a distinctive lower/upper arm subchain, including a rotational "elbow" joint and "shoulder" and "wrist" joints with offsets, as shown in Fig. 1. The satellite dimensions and manipulator attachment position are similar to these of ETS VII, see Fig. 2. The dynamic parameters are shown in Table I. The offsets at the shoulder and wrist joints are needed to attain the stowed configuration. Also, these offsets are regarded as essential for the proposed reactionless tasks discussed in Section IV.

B. Reactionless motion analysis

Before proceeding with the proposal of practical reactionless motion tasks, we should discuss reactionless motion with our manipulator model. For the sake of simplicity, we divide the kinematic structure into positioning and wrist subchains. The positioning subchain consists of Joints 1 through 4, the rest of the joints constitute the wrist subchain.

First, we consider rotational motion of the end-effector under reactionless motion control. The orientation of the

TABLE I

DYNAMIC MODEL PARAMETERS

	Mass [kg]	Inertia moment [kgm^2]		
i	m_i	I_{xi}	I_{yi}	I_{zi}
1	30.0	0.0671	0.0671	0.0851
2	30.0	0.0843	0.267	0.267
3	45.0	3.81	3.81	0.127
4	40.0	0.113	2.19	2.19
5	20.0	0.213	0.213	0.0250
6	20.0	0.0250	0.0292	0.0292
7	25.0	0.0990	0.0990	0.0313

end-effector is usually controlled by the wrist subchain. It should be intuitively clear that because of the relatively small mass and inertia of the wrist assembly, the disturbance of the base due to wrist motion will be far smaller than that due to motion in the positioning subchain. Hence, the orientation of the end-effector could be controlled within a relatively large area under reactionless motion, with respective compensating motion by the positioning subchain. It is important to note, though, that without reactionless motion, the disturbance induced by wrist motion cannot be ignored, as will be demonstrated in what follows.

In contrast to orientation, linear path tracking with the end-effector under reactionless motion is more complex. As mentioned in Section II-B, the linear motion constraint frequently leads to the occurrence of algorithmic singularities. Therefore, our approach is to consider the entire motion of the manipulator rather than solely the end-effector motion. Note that the manipulator motion is largely related to the motion of the positioning subchain. Hence, we will focus on reactionless motion with this subchain. Then, the dimension of the null space of the coupling inertia matrix is reduced to one, and the parameterization of reactionless motion is simplified.

Considering the nature of angular momentum conservation, it is apparent that motions in the joint that lead to large disturbances of the base should be suppressed as much as possible. In our model, motions in Joints 1 and 2 induce such disturbances because they significantly affect the movement of the CoM of the manipulator. Hence, the involvement of these joints in reactionless motion should be avoided as much as possible. Which means that the remaining Joints 3 and 4 of the positioning chains are to be preferred when generating such motion. Indeed, from empirically obtained results with several initial configurations, we were able to confirm that reactionless motion is almost exclusively composed of motion in Joint 4, with a minor contribution in Joint 3. Two examples are displayed in Fig. 3: Fig. 3 (a) shows a frequently observed reactionless motion pattern; Fig. 3 (b), on the other hand, is a special case obtained when the initial configuration is in the vicinity of $\theta_2 = 0$. Hence, we will consider only cases that avoid such initial configurations.

We can conclude that representative reactionless motion are the wrist motion and the Joint 4 motion, with a subtle Joint 3 motion. We will refer to the latter motion as the *reactionless folding/unfolding motion*, because it results mainly from the elbow joint (Joint 4).

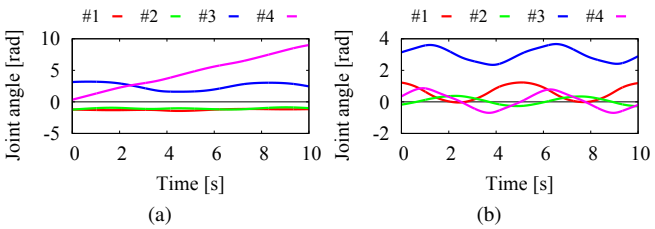

Fig. 3. Representative reactionless motion patterns obtained with the positioning subchain: (a) major motion pattern and (b) minor motion pattern. The later pattern only appears around $\theta_2 = 0$ rad.

IV. PROPOSAL OF PRACTICAL REACTIONLESS MOTION TASKS

In this section, we propose three practical task candidates to be executed under reactionless motion, as specified in the previous section. The first candidate is an inspection task using the end-effector hand camera. The second one is a manipulator deployment/stowing maneuver. The third one is a general PTP motion task.

A. Reactionless inspection using the hand camera

One frequent task for free-floating space robots is inspection of various devices mounted on satellites or large space structures, with a camera attached to the end-effector. Such task was also performed within the ETS-VII mission [18]. Once the arm is positioned appropriately, the camera view angle for inspection is changed by rotating the wrist. This task is a good candidate for a reactionless maneuver since the hand camera is assumed to be lightweight.

It would be straightforward to realize a reactionless wrist rotation using (6). Note however, that the position of the wrist is uncontrolled and may largely deviate from the initial one. This is not desirable since the camera may collide with other equipment. In fact, such experiment was performed during a PTP positioning maneuver with the ETS-VII manipulator [5]. The position of the wrist was calculated off-line and then uploaded for execution, but only after making sure that the generated path is collision-free. It is clear that such approach is not practical.

To alleviate the above problem, we modify (6) by adding an addtional constraint. Consider the following cost function:

$$V = \frac{1}{2}(\boldsymbol{x}_W^{init} - \boldsymbol{x}_W(t))^T \boldsymbol{\Lambda} (\boldsymbol{x}_W^{init} - \boldsymbol{x}_W(t)) \qquad (7)$$

where $\boldsymbol{x}_W$, $\boldsymbol{x}_W^{init} \in \mathbb{R}^3$ denote current and initial wrist position and $\boldsymbol{\Lambda} \in \mathbb{R}^{3\times3}$ is a diagonal weight matrix. To minimize the cost function, we employ a vector from the null-space of matrix $\boldsymbol{G}_\omega = [\tilde{\boldsymbol{M}}_{\omega m}^T \ \boldsymbol{J}_{E\omega}^T]^T \in \mathbb{R}^{6\times7}$ as a gradient vector for the cost function. Consequently, the reference joint velocity is obtained in the following form:

$$\dot{\boldsymbol{\theta}}^{ref} = \boldsymbol{G}_\omega^+ \begin{bmatrix} \boldsymbol{0} \\ \boldsymbol{\omega}_E^{ref} \end{bmatrix} + k_g \boldsymbol{P}_{G_\omega} \boldsymbol{J}_{Wv}^T (\boldsymbol{x}_W^{init} - \boldsymbol{x}_W(t)) \qquad (8)$$

where $\boldsymbol{P}_{G_\omega} = \boldsymbol{E} - \boldsymbol{G}_\omega^+ \boldsymbol{G}_\omega \in \mathbb{R}^{7\times7}$ denotes a projector onto the null space of $\boldsymbol{G}_\omega$, $\boldsymbol{J}_{Wv} \in \mathbb{R}^{3\times7}$ stands for the Jacobian with respect to the wrist linear velocity, k_g is a scalar gradient gain. Note that the frequency of arriving at algorithmic singularity with this formulation is approximately the same as the

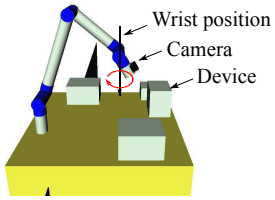

Fig. 4. Desired motion for inspecting a surface-mounted device.

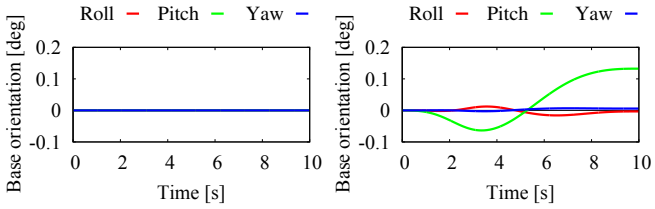

Fig. 5. Comparison results of inspection maneuver: (a) reactionless motion control and (b) nominal control method.

occurrence of wrist kinematic singularities. Nevertheless, it is advisable to employ singularity treatment techniques, such as the Singularity-Consistent method [19], [20] for example. Also, care should be taken to avoid stationary-point type local minima of the null-space gradient optimization.

In what follows, we examine the performance under (8) by comparison to the conventional inverse kinematic controller $\dot{\boldsymbol{\theta}}^{ref} = \boldsymbol{J}_{E\omega,W}^{-1}\boldsymbol{\omega}_E^{ref}$, via numerical simulations. $\boldsymbol{J}_{E\omega,W} \in \mathbb{R}^{3\times3}$ stands for the Jacobian composed of the wrist subchain. We assume the task of inspecting a device mounted on the satellite surface, as shown in Fig. 4. The initial configuration is set as $[90\ -20\ 180\ 110\ 0\ 20\ 0]^T$ deg, the reference angular velocity is $\boldsymbol{\omega}_E^{ref}(t) = \dot{\alpha}^{ref}(t)[0\ 0\ -1]^T$ rad/s, where $\alpha^{ref}(t) = s(t)\pi$ generates the desired wrist rotation around the rotational axis, $0 \leq s(t) \leq 1$ denoting a fifth-order polynomial function.

The simulation results are displayed in Fig. 5 and Fig. 6. These are obtained with $k_g = 100$, the weight matrix set as the identity matrix. From the results in Fig. 5 (a) it is seen that, with the proposed method, the rotation of the end-effector can be accomplished without inducing reactions to the base. In contrast, a relatively large base orientation change can be observed under the conventional control method, despite the low inertia parameters of the wrist (see Fig. 5 (b)). From the wrist deflection graph in Fig. 6 it becomes apparent that the effect of the cost function leads to a sufficiently small deviation from the initial wrist position. Hence, we can conclude that this motion maneuver is applicable as an inspection maneuver using the hand camera.

B. Reactionless manipulator deployment from the stowed configuration

When launching a free-floating space robot into orbit, the manipulator has to be stowed. The *stowed configuration* is shown in the upper left part of Fig. 7. During on-orbit experiments, deploying and stowing of a manipulator is executed multiple times [13]. Hence, this task is a good

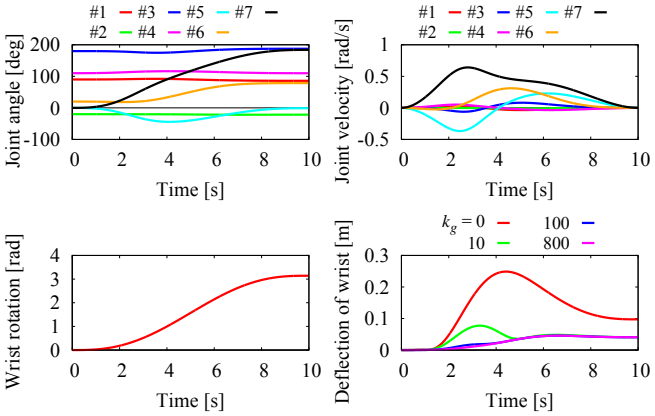

Fig. 6. Camera inspection maneuver with reactionless end-tip orientation control. The deflection of the wrist position from the initial one can be made sufficiently small via the gradient gain k_g.

candidate for reactionless motion control, when aiming at improved mission efficiency.

We use the reactionless folding motion with the positioning subchain, as described in the previous section. The angular momentum conservation constraint (3) is then modified as $\tilde{\boldsymbol{M}}_{\omega m,P}\dot{\boldsymbol{\theta}}_P = \boldsymbol{0}$, where $\tilde{\boldsymbol{M}}_{\omega m,P} \in \mathbb{R}^{3\times4}$ is a submatrix of $\tilde{\boldsymbol{M}}_{\omega m}$ related to the positioning subchain, $\boldsymbol{\theta}_P$ stands for the joint coordinate vector of that chain. The reactionless folding/unfolding motion can be generated via the following equation:

$$\dot{\boldsymbol{\theta}}_P^{ref} = \begin{bmatrix} -\tilde{\boldsymbol{M}}_{123}^{-1}\tilde{\boldsymbol{M}}_4 \\ 1 \end{bmatrix} \dot{\theta}_4^{ref}, \tag{9}$$

where $\tilde{\boldsymbol{M}}_{123} \in \mathbb{R}^{3\times3}$ and $\tilde{\boldsymbol{M}}_4 \in \mathbb{R}^{3\times1}$ are submatrices of $\tilde{\boldsymbol{M}}_{\omega m,P}$. The subscripts indicate the relation to the respective joints.

Further on, since only the four joints of the positioning chain are employed, the dimension of the RNS is one. Therefore, the reactionless motion path is uniquely determined by the initial (stowed) configuration. The final (deployed) configuration can be selected as any configuration along the reactionless path. The selection will depend upon the subsequent task. Careful planning for the stowed/deployed configurations is needed. The benefit is that the speed/acceleration along the reactionless path connecting the two configurations can be set freely which allows for a very time-efficient deployment.

We denote the candidates for the stowed configuration of our model as follows:

$$\boldsymbol{\theta}_{st} = \{\boldsymbol{\theta} \in \mathbb{R}^7 \,|\, \theta_i = \pm\pi/2, \theta_j = 0, \pm\pi, \forall\theta_7\} \\ (i = 1, 2, j = 3 \text{ to } 6). \tag{10}$$

We pick up a configuration that is well-conditioned for the deployment maneuver: $[\pi/2\ \ -\pi/2\ 0\ \ -\pi\ \pi\ \pi\ 0]^T$ rad. Snapshots from the deployment sequence are shown in Fig. 7, base deflection and joint angle data are presented in Fig. 8. It can be seen that the final configuration is quite appropriate as an inspection configuration. Hence, it is possible to execute an inspection maneuver immediately after deploying.

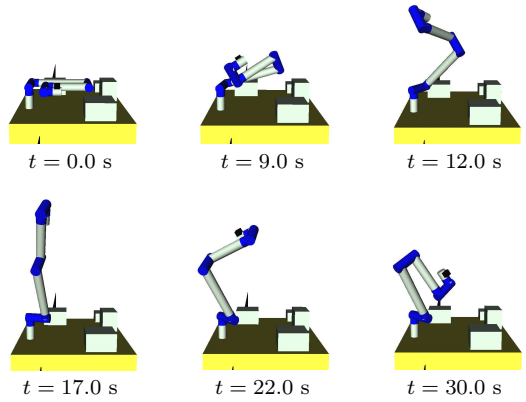

Fig. 7. Motion snapshots from the deployment maneuver under reactionless motion control.

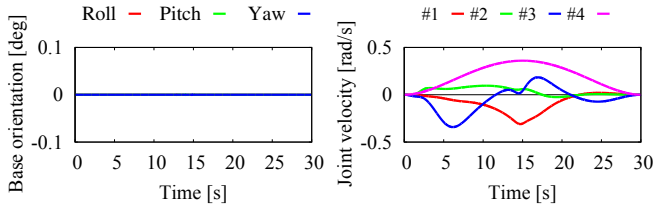

Fig. 8. Simulation results from the deployment maneuver under reactionless motion control.

C. PTP maneuver with partial reactionless motion

PTP motion maneuvers are widely used. Due to the reasons outlined above, we restrict our attention to a specific subset of PTP maneuvers: arm reconfiguration tasks wherein the hand does not hold an object. It would be desirable to execute such maneuvers under reactionless motion control. This, however, is impossible for arbitrary points since reactionless motions are quite restricted, as already explained. Nevertheless, reactionless motion can be useful, if the PTP motion is planned appropriately. One possibility is to combine a reactionless motion with a conventional PTP motion. Another possibility is to divide the motion into two reactionless motions and one conventional motion. This method has been referred to as the *3-phase method* and applied to a planar flexible-base robot [15]. From this study, it became apparent that the method can be used for motions with large displacements. The method has not been verified for the case of a free-floating robot. Below we show how to adopt the 3-phase method to PTP motion with our three-dimensional free-floating model. Before doing so, we will review the 3-phase method briefly.

1) 3-phase method: The joint path that connects the specific initial and final configurations is designed by connecting three sub-paths. In Fig. 9, Paths A and C are reactionless paths. Path B is a conventional (non-reactionless) PTP path used to connect the two reactionless motion paths. The primary concern is how to determine the three sub-paths to obtain the smallest possible base reaction during the PTP sub-path (Path B). In [15], a folded-arm configuration is used for Path B as this configuration induces small reaction due to the property of the flexible-base model.

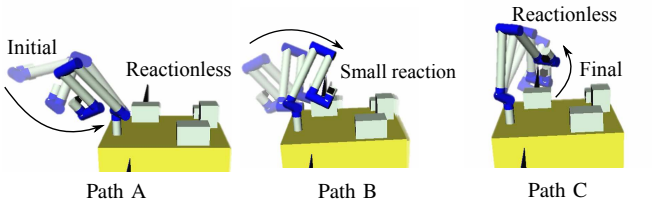

Fig. 9. 3-phase method: PTP maneuver with partial reactionless paths.

In general, it is desirable to obtain the optimal path for reaction minimization during the second phase (Path B). However, because of the high dimension and the nonlinearity of the system, it is difficult to obtain the optimal solution. Therefore, we adopt here the folded-arm configuration as a suitable configuration during the second phase. Recall that the folding/unfolding of the arm can be always done along reactionless paths. We provide a theoretical argument of reaction reduction with the folded configuration in what follows.

The coupling angular momentum can be rewritten in the following form:

$$\tilde{\boldsymbol{M}}_{\omega m}\dot{\boldsymbol{\theta}} = \Big\{\sum_{i=1}^{7} \boldsymbol{I}_i \boldsymbol{J}_{\omega i}\Big\}\dot{\boldsymbol{\theta}} + \Big\{\sum_{i=1}^{7} m_i [\boldsymbol{r}_i^{\times}] \boldsymbol{J}_{vi}\Big\}\dot{\boldsymbol{\theta}} - \Big\{m_C [\boldsymbol{r}_C^{\times}] \boldsymbol{J}_C\Big\}\dot{\boldsymbol{\theta}}, \qquad (11)$$

where $\boldsymbol{I}_i \in \mathbb{R}^{3\times 3}$ is the link inertia tensor, $\boldsymbol{J}_{vi}$, $\boldsymbol{J}_{\omega i} \in \mathbb{R}^{3\times n}$ are the Jacobian matrices w.r.t. the linear and angular velocity of each link, $\boldsymbol{r}_i$ and $\boldsymbol{r}_C \in \mathbb{R}^3$ are position vectors of the CoM of each link and the whole system w.r.t. base frame, m_i and m_C denote masses of each link and the whole system, respectively. $(\circ)^{\times}$ stand for a skew-symmetric matrix for the respective vector.

It is apparent that the coupling angular momentum consists of two components. The first one is the angular momentum stemming from the rotational motion of each link, i.e. the first term on the r.h.s. of (11). The second one is the angular momentum due to the translational motion of the CoM of each link, i.e. the second and third terms. These two components are smallest when the manipulator is folded, for the following reasons. First, in the case of rotational motion, the inertia tensor of the manipulator is smallest when the manipulator is folded. Hence, the rotational reaction can be reduced. Next, from the second and third term in (11) it is seen that the translational reaction is related to the CoM position of each link. In the folded configuration, the manipulator CoM is closest to the CoM of the base and the linear velocity becomes small. As a result, the translational reaction can be also reduced. For these reasons, in this work we use the folded configuration during Path B.

2) Verification via simulations: The reference motion is shown in Fig. 9. The initial configuration is $[300\ -40\ 0\ -60\ 180\ 180\ 0]^T$ deg, the final one is $[140\ 10\ 0\ -100\ 180\ 180\ 0]^T$ deg. These two configurations cannot be linked via a reactionless path. Therefore, we apply the 3-phase method. Path A is a reactionless motion path from

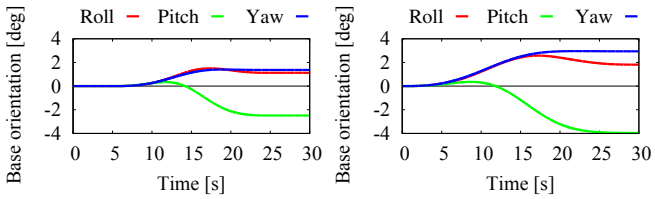

Fig. 10. Comparison result of base orientation deviation: (a) partial reactionless PTP motion and (b) conventional PTP motion.

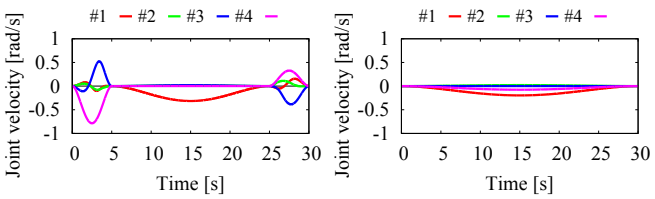

Fig. 11. Time profile of joint velocity of each method: (a) partial reactionless PTP motion and (b) conventional PTP motion.

the initial configuration toward folded arm configuration FA-1. Path C is determined from a reversed reactionless motion starting from the final configuration toward folded-arm configuration FA-2. The two folded-arm configurations are distinct and uniquely defined as resultant configurations along the respective reactionless paths, wherein $\theta_4 = -\pi$ rad. In the simulation, paths A and C are executed in 5 seconds, and Path B in 20 seconds. It should be noted that the reactionless folding motions can be executed under the condition described in Section III.

Simulation results are shown in Fig. 10, Fig. 11. It is apparent that base orientation changes within Path B only. For comparison, we simulate a conventional PTP motion which links the two configurations via a fifth-order polynomial function. It is seen that with the 3-phase method, the deviation of the base orientation is smaller than that under the conventional PTP motion. In particular, the deviation of the pitch axis for the proposed motion is half as small as that of the conventional one. Note that, along the reactionless paths, the joint rates can be scaled so that the maximum joint rate can be reached for certain joints, that would further increase the efficiency. From these results, we can conclude that the 3-phase motion maneuver can be used in practice.

V. Conclusion

We tackled the problem of how to apply reactionless motion in practical tasks, with a realistic model of a seven-DoF redundant manipulator. We have shown that for the specific manipulator structure, which is quite common, reactionless motion can be obtained as a folding/unfolding motion via the elbow joint, and as a wrist motion. Using these motions, we suggested three reactionless maneuvers as follows: (i) inspection maneuver using the end-effector hand camera, (ii) extension maneuver from the stowed configuration and (iii) point-to-point motion maneuver with partial reactionless motion. From the verification via numerical simulations, it was clarified that these maneuvers can be applied for practical tasks.

References

[1] Z. Vafa and S. Dubowsky, "On the dynamics of manipulators in space using the virtual manipulator approach," in *Proc. IEEE Int. Conf. Robot. Autom.*, 1987, pp. 579–585.

[2] D. Nenchev, K. Yoshida, and Y. Umetani, "Introduction of redundant arms for manipulation in space," in *IEEE Int. Workshop on Intelligent Robots*, 1988, pp. 679–684.

[3] A. Gouo, D. N. Nenchev, K. Yoshida, and M. Uchiyama, "Motion control of dual-arm long-reach manipulators," *Advanced Robotics*, vol. 13, no. 6, pp. 617–631, 1998.

[4] K. Yoshida, K. Hashizume, D. Nenchev, N. Inaba, and M. Oda, "Control of a space manipulator for autonomous target capture - ETS-VII flight experiments and analysis," in *Proc. AIAA Guidance, Navigation, and Control Conference and Exhibit*, AIAA2000–4376, 2000.

[5] K. Yoshida, K. Hashizume, and S. Abiko, "Zero reaction maneuver: flight validation with ETS-VII space robot and extension to kinematically redundant arm," in *Proc. IEEE Int. Conf. Robot. Autom.*, 2001, pp. 441–446.

[6] S. Abiko and K. Yoshida, "Adaptive reaction control for space robotic applications with dynamic model uncertainty," *Advanced Robotics*, vol. 24, no. 8-9, pp. 1099–1126, 2010.

[7] T.-C. Nguyen-Huynh and I. Sharf, "Adaptive reactionless motion for space manipulator when capturing an unknown tumbling target," in *Proc. IEEE Int. Conf. Robot. Autom.*, 2011, pp. 4202–4207.

[8] S. V. Shah, I. Sharf, and A. Misra, "Reactionless path planning strategies for capture of tumbling objects in space using a dual-arm robotic system," in *Proc. AIAA Guidance, Navigation, and Control (GNC) Conference*, 2013.

[9] D. Hirano, Y. Fujii, S. Abiko, R. Lampariello, K. Nagaoka, and K. Yoshida, "Simultaneous control for end-point motion and vibration suppression of a space robot based on simple dynamic model," in *Proc. IEEE Int. Conf. Robot. Autom.*, 2014, pp. 6631–6637.

[10] N. Hara, D. Nenchev, and D. Sato, "Momentum conserving path tracking through dynamic singularities with a flexible-base redundant manipulator," in *Proc. IEEE/RSJ Int. Conf. on Intelligent Robots and Systems*, 2010, pp. 5392–5397.

[11] S. K. Agrawal and A. Fattah, "Reactionless space and ground robots: Novel designs and concept studies," *Mechanism and Machine Theory*, vol. 39, no. 1, pp. 25–40, 2004.

[12] M. Carpenter and M. Peck, "Reducing base reactions with gyroscopic actuation of space-robotic systems," *IEEE Transactions on Robotics*, vol. 25, no. 6, pp. 1262–1270, 2009.

[13] T. J. Debus and S. P. Dougherty, "Overview and performance of the front-end robotics enabling near-term demonstration (FREND) robotic arm," in *Proc. AIAA Unmanned Unlimited Conference*, 2009, pp. 1–12.

[14] D. Nenchev and K. Yoshida, "Impact analysis and post-impact motion control issues of a free-floating Space robot subject to a force impulse," *IEEE Trans. Robot. Autom.*, vol. 15, no. 3, pp. 548–557, 1999.

[15] K. Yoshida, D. N. Nenchev, P. Vichitkulsawat, H. Kobayashi, and M. Uchiyama, "Experiments on the point-to-point operations of a flexible structure mounted manipulator system," *Advanced Robotics*, vol. 11, no. 4, pp. 397–411, 1996.

[16] Y. Masutani, F. Miyazaki, and S. Arimoto, "Sensory feedback control for space manipulators," in *Proc. IEEE Int. Conf. Robot. Autom.*, 1989, pp. 1346–1351.

[17] K. Yoshida, "Engineering test satellite VII flight experiments for space robot dynamics and control: theories on laboratory test beds ten years ago, now in orbit," *The International Journal of Robotics Research*, vol. 22, no. 5, pp. 321–335, 2003.

[18] M. Oda, K. Kibe, and F. Yamagata, "ETS-VII, space robot in-orbit experiment satellite," in *Proc. IEEE Int. Conf. Robot. Autom.*, 1997, pp. 739–744.

[19] D. N. Nenchev and K. Yoshida, "Singularity-Consistent teleoperation techniques for redundant free-flying robots," in *Proc. AIAA Guidance, Navigation, and Control Conference,*, 1999, pp. 1895–1902.

[20] S. Taki and D. Nenchev, "A novel Singularity-Consistent inverse kinematics decomposition for S-R-S yype manipulators," in *Proc. IEEE Int. Conf. Robot. Autom.*, 2014, pp. 5070–5075.